

Phase diagram of $J_1 - J_2$ transverse field Ising model on the checkerboard lattice: a plaquette-operator approach

M. Sadrzadeh¹ and A. Langari^{1,2,3}

¹*Department of Physics, Sharif University of Technology, P.O.Box 11155-9161, Tehran, Iran**

²*Center of excellence in Complex Systems and Condensed Matter (CSCM), Sharif University of Technology, Tehran 145889694, Iran*

³*Max-Planck-Institut für Physik komplexer Systeme, 01187 Dresden, Germany*

(Dated: May 14, 2019)

We study the effect of quantum fluctuations by means of a transverse magnetic field (Γ) on the antiferromagnetic $J_1 - J_2$ Ising model on the checkerboard lattice, the two dimensional version of the pyrochlore lattice. The zero-temperature phase diagram of the model has been obtained by employing a plaquette operator approach (POA). The plaquette operator formalism bosonizes the model, in which a single boson is associated to each eigenstate of a plaquette and the inter-plaquette interactions define an effective Hamiltonian. The excitations of a plaquette would represent an-harmonic fluctuations of the model, which lead not only to lower the excitation energy compared with a single-spin flip but also to lift the extensive degeneracy in favor of a plaquette ordered solid (RPS) state, which breaks lattice translational symmetry, in addition to a unique collinear phase for $J_2 > J_1$. The bosonic excitation gap vanishes at the critical points to the Néel ($J_2 < J_1$) and collinear ($J_2 > J_1$) ordered phases, which defines the critical phase boundaries. At the homogeneous coupling ($J_2 = J_1$) and its close neighborhood, the (canted) RPS state, established from an-harmonic fluctuations, lasts for low fields, $\Gamma/J_1 \lesssim 0.3$, which is followed by a transition to the quantum paramagnet (polarized) phase at high fields. The transition from RPS state to the Néel phase is either a deconfined quantum phase transition or a first order one, however a continuous transition occurs between RPS and collinear phases.

PACS numbers: 75.10.Jm, 75.30.Kz, 64.70.Tg

I. INTRODUCTION

Frustrated magnetic systems imply large degenerate classical configurations as a groundstate subspace, which could lead to novel phases and exotic features like emergent magnetic monopoles in spin ice¹. Quantum fluctuations as perturbations may select one of these degenerate states as a unique quantum ground-state of the system representing unusual ordering. Besides the magnetic properties, which are described by models of frustrated systems, such models mimic some features of unconventional superconductivity in terms of resonating valence bond (RVB) phase² on the triangular lattice³⁻⁶, governed by quantum dimer model (QDM)⁷. The RVB scenario has received a great impact to elucidate the plaquette RVB phase in the $s=1/2$ honeycomb $J_1 - J_2$ Heisenberg model^{8,9}, which is justified by the two-dimensional approach of density matrix renormalization group, recently^{10,11}. It gives the impression that the plaquette type ordered phase is a result of strong correlation and frustration, which has also been observed in the square lattice¹²⁻¹⁶. According to Ref.¹⁵, which shows that a plaquette phase is stable in the range of parameters, where a spin-liquid phase has been reported^{16,17}, it is interesting to investigate the spin-liquid phase within a plaquette operator approach.

The three-dimensional pyrochlore lattice is a fascinating example of geometrically frustrated lattices, which has a two-dimensional (2D) version called checkerboard lattice (see Fig. 1). Quantum Heisenberg model has been widely studied on checkerboard lattice, where degeneracy of the groundstate is lifted toward a unique non-magnetic ordered state, which is called a plaquette ordered phase or a plaquette valence bond solid (pVBS). This state does not break $SU(2)$ symmetry and

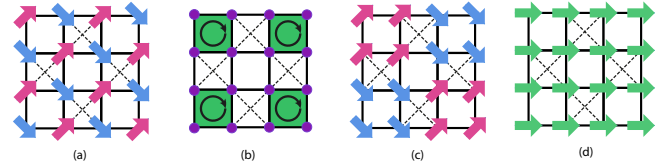


FIG. 1. (color online) Schematic representations for various phases of the $J_1 - J_2$ transverse field Ising model on the checkerboard lattice. The solid and dashed lines are J_1 and J_2 bonds, respectively. (a) The (canted) Néel state, (b) the (canted) RPS state, (c) the (canted) collinear state and (d) the quantum paramagnet (polarized) state.

is gapped but breaks the space symmetry of the lattice¹⁸⁻²⁷.

However, the reduction of symmetry from $SU(2)$ to Z_2 renders the antiferromagnetic Ising model on the checkerboard lattice as a prototype of frustrated systems, which gives interesting features. At the isotropic coupling $J_2 = J_1$, the Ising model on the checkerboard lattice has an extensive degenerate ground state defined by *ice-rule* manifold, i.e. 'two-in-two-out' on crossed squares, which imitates a classical spin liquid known as square ice. Quantum fluctuations lift the degeneracy of the manifold toward a single magnetic⁵ or non-magnetic plaquette ordered state^{28,29}. In Ref.²⁸, the ice-rule manifold is mapped to the spin configurations of quantum six-vertex model. The quantum fluctuations of a weak in-plane XY-term are considered in terms of the second order perturbation on the ice-rule manifold, which leads to cyclic cluster terms that can be modeled by a QDM of flippable plaquettes, which stabilizes a plaquette phase at zero chemical potential^{28,30}. However, in this article we show explicitly the existence of a resonating plaquette solid state in terms of its corresponding or-

der parameter, which will be introduced. Moreover, we indicate the region, where an RPS state is being formed in the neighborhood of $J_2 = J_1$ of our phase diagram.

We study a general transverse field Ising model (TFIM) on the checkerboard lattice:

$$\mathcal{H} = J_1 \sum_{\langle i,j \rangle} S_i^z S_j^z + J_2 \sum_{\langle\langle i,j \rangle\rangle} S_i^z S_j^z - \Gamma \sum_i S_i^x \quad (1)$$

where $J_1 > 0$ is the nearest neighbor coupling, $J_2 > 0$ is the diagonal coupling on crossed squares, Γ is the strength of transverse magnetic field and $S^{x,z}$ refer to x and z components of spin-1/2 operators on the vertices of the lattice. In the absence of transverse field Γ , as well as exponentially degenerate groundstate (with the system size) of the isotropic case $J_2 = J_1$, there is exponentially degenerate groundstate with the linear size of the system for $J_1 < J_2$ (the collinear phase) and a unique groundstate (although with a Z_2 degeneracy) for $J_1 > J_2$ (the Néel phase).

Recently, the transverse field Ising model on the $J_1 - J_2$ checkerboard lattice has been studied within linear spin-wave theory (LSWT)³¹. The phase diagram consists of three phases, Néel ordered for low magnetic field and $J_2 < J_1$, highly degenerate collinear phase at low field and $J_2 > J_1$ and fully polarized phase for high transverse fields (Γ). Based on harmonic fluctuations considered in Ref.³¹, the boundary between Néel and collinear phases is at $J_2 = J_1$ for $0 \leq \Gamma \lesssim 0.7$ without an indication of an RPS phase, which is a witness for the break down of LSWT. Moreover, the border for the polarized-Néel and polarized-collinear phase transitions can not be determined accurately within LSWT due to strong quantum fluctuations, leading to instabilities close to the phase boundaries³¹.

The first clue to solve the problem is to employ the proper building blocks, which incorporate the correct ingredients of the ground state structure and the elementary excitations of the model. At zero field and in the intermediate regime i.e. for $2/3 < J_2/J_1 < 4/3$, where the role of frustration is important, a plaquette flip excitation has lower energy than a single spin-flip³¹, which suggests that the true excitations of the model is governed by a plaquette flip that is a representation of an-harmonic fluctuations (of the original spin model). Moreover, the zeroth-order calculations of the ground state energy immediately justify that a single plaquette background gives lower value than a single particle classical background. We implement a plaquette-operator approach (POA)^{32,33}, which is an extension of the bond-operator theory³⁴ to obtain the zero temperature phase diagram of $J_1 - J_2$ TFIM on the checkerboard lattice, accurately. We explicitly find the quantum phase boundary for paramagnet-Néel and paramagnet-collinear transitions, where the excitation energy of bosonic quasi-particles vanishes as the onset of a Bose-Einstein condensation. The corresponding phase diagram is presented in Fig. 11. Moreover, we show that an-harmonic fluctuations lift the extensive degeneracy of the collinear phase to form a unique quantum state of collinear order. In addition, the phase transition between Néel and collinear phases only appears at zero field ($\Gamma = 0$) and $J_2 = J_1$ while for small field region a (canted) RPS phase fills the phase diagram. The

RPS phase breaks the translational symmetry of the lattice, which has twofold degeneracy. The increment of transverse field causes a transition from the (canted) RPS phase to the quantum-paramagnet one.

Our paper is organized as follows: In sec. II we describe the plaquette operator approach applied for TFIM on the checkerboard lattice. We obtain and discuss the POA results and compare them with LSWT ones in Sec. III. Finally, we summarize and conclude in sec. IV. Some details of our calculations of the groundstate energy, correlations, and the order parameters can be found in Appendix 1, Appendix 2 and Appendix 3, respectively.

II. PLAQUETTE OPERATOR APPROACH

The plaquette operator approach is an extension of the bond-operator formalism³⁴, where the bond is replaced by a cluster of spins, namely: plaquette. In the bond-operator approach, a pair of spins – a bond – is treated exactly and a bosonic operator is associated to each eigenstate of the bond. A condensation for the lowest (energy) boson is considered as the background configuration of the model. The effect of inter-bond interactions is taken into account perturbatively in terms of boson operators, which defines the effective theory for the original spin model. The ground state energy is minimized self consistently, which includes the corrections caused by the quantum fluctuations of quasi-particle bosons. To preserve the Hilbert space, a constraint has to be imposed on the boson occupation of each bond, i.e. the total occupation of all bosons on a single bond have to be equal to unity.

In the plaquette operator approach the system is divided to a set of individual plaquettes that are shaded as one every two uncrossed squares of the checkerboard lattice (see Fig. 1-(b)). The total Hamiltonian, Eq. 1, is written as $\mathcal{H} = \mathcal{H}_0 + \mathcal{H}_{int}$, where \mathcal{H}_0 denotes the Hamiltonian for the set of non-corner-sharing uncrossed squares, called plaquettes, and \mathcal{H}_{int} represents the interaction between plaquettes. The plaquette Hamiltonian (\mathcal{H}_0) is solved exactly and its lowest eigenstate is subjected to the Bose-condensation that defines the system background. The elementary excitations are of a plaquette type, which are created as a consequence of inter-plaquette interactions (\mathcal{H}_{int}) out of the Bose-condensated background. The ground state energy is corrected by considering the inter-plaquette interactions, which leads to the proper quasi-particle excitations of the model that determine the critical phase boundaries at the location of vanishing of the energy gap.

A. A single plaquette

The Hamiltonian of a single plaquette is in the following form (the scale of energy is set by $J_1 = 1$):

$$\mathcal{H}_P = \sum_{\langle i,j \rangle} S_i^z S_j^z - \Gamma \sum_i S_i^x \quad (2)$$

where $i, j = 1, 2, 3, 4$ are the indices of the four spins located on the corners of a plaquette (see Fig. 4). Hence, \mathcal{H}_0 is a sum

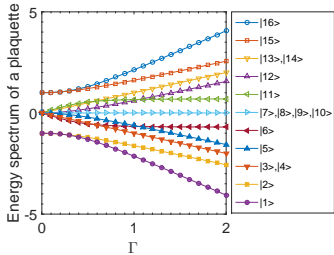


FIG. 2. (color online) Energy levels, in units of J_1 , of a single plaquette versus transverse field (Γ). The levels ($|3\rangle, |4\rangle$), ($|13\rangle, |14\rangle$) and ($|7\rangle, |8\rangle, |9\rangle, |10\rangle$) are degenerate. The bottom (\bullet) line is the unique groundstate of the plaquette.

on all (non-corner sharing) plaquettes, i.e. $\mathcal{H}_0 = \sum_P \mathcal{H}_P$. The single-plaquette Hamiltonian is diagonalized exactly and its energy spectrum versus transverse field Γ is plotted in Fig. 2. We see that the ground state of a plaquette is non-degenerate except for $\Gamma = 0$. Hence, in a non-zero transverse field and in the absence of interaction between plaquettes, all of the isolated plaquettes are in their unique groundstates.

The zeroth order approximation gives an impression on how a plaquette background (\mathcal{H}_0) would lead to a proper approximation for the ground state energy. In Fig. 3 we have compared the ground state energy of the classical approximation – that has been used as the background configuration in LSWT³¹ – with the ground state energy of the quantum plaquette order (\mathcal{H}_0), which is employed as a background in POA (the present work). Accordingly, the following two facts can be deduced. (i) The ground state energy of a plaquette is lower than the classical one for high-field values, Fig. 3-(a). It shows that POA is a high-field approach within the chosen plaquettes of Fig. 1-(b). Thus, we expect to get reasonable excitations of the model for high field values and arrive at a gapless critical point by reducing the transverse field for a fixed value of the exchange coupling J_2 . (ii) For the intermediate region of the exchange coupling, namely: $J_2 \sim J_1$, where the frustration prohibits that all bonds being minimized classically, the dominant term is the transverse field compared with the frustrated exchange ones even at low field values, see Fig. 3-(b). It suggests that we should expect acceptable results for the low transverse fields close to the highly frustrated regime $J_1 \sim J_2$.

The inter-plaquette interactions excite the plaquettes to the higher eigenstates, which reduces the probability of a single plaquette to be in its groundstate. The quantum fluctuations caused by the inter-plaquette interactions modify the ground state energy and render the proper excitations of the model to govern the critical boundaries.

B. Interaction between plaquettes: a bosonic representation

The inter-plaquette Hamiltonian, $\mathcal{H}_{int} = \mathcal{H} - \mathcal{H}_0$, which is composed of Ising terms on the dotted and dashed links of Fig. 4, does not commute with the plaquette Hamiltonian \mathcal{H}_0 that includes the transverse field. As a result, the inter-plaquette interactions hybridize the ground state of a single

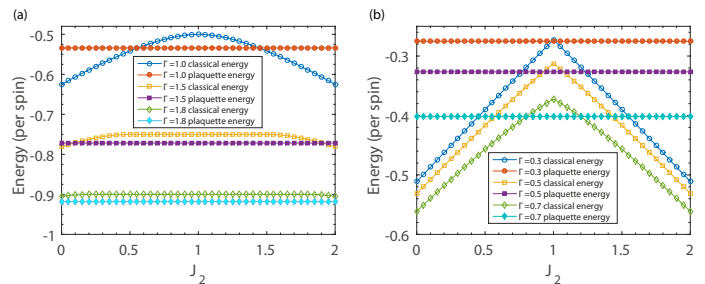


FIG. 3. (color online) Ground state energy (per spin) versus J_2 at fixed values of the transverse magnetic field. (a) $\Gamma = 1.0, 1.5, 1.8$ and (b) $\Gamma = 0.3, 0.5, 0.7$. For each value of Γ the open symbol shows the classical ground state energy and the filled one corresponds to the quantum plaquette order (\mathcal{H}_0).

plaquette with the corresponding excited eigenstates. In order to take into account the effect of inter-plaquette interactions, we implement a bosonization formalism³³ similar to what has been introduced as bond-operator representation of spin systems^{34–39}. A boson is associated to each eigenstate $|u\rangle$ of a single-plaquette Hamiltonian such that the eigenstate is created by the corresponding boson creation operator $b_{I,u}^\dagger$ acting on the vacuum,

$$|u\rangle_I = b_{I,u}^\dagger |0\rangle, \quad u = 1, \dots, 16, \quad (3)$$

where I denotes the plaquette label of a shaded square of Fig. 1-(b). The bosonic operators b_u^\dagger and b_u obey the known commutation relation $[b_u, b_u^\dagger] = 1$.

In the absence of inter-plaquette interactions, all of the isolated plaquettes are in their groundstates, $|1\rangle$. Therefore, a plaquette ordered state can be defined as a Bose-condensation of the groundstate bosons. We assign a Bose-condensation amplitude \bar{p}_I ,

$$\bar{p}_I^2 \equiv \langle b_{I,1}^\dagger b_{I,1} \rangle, \quad (4)$$

which gives the probability of a single plaquette to be in its ground state. For simplicity and within a mean-field level of approximation we consider

$$b_{I,1} \equiv b_{I,1}^\dagger \equiv \bar{p}, \quad (5)$$

for all plaquettes, which is equal to unity in the absence of inter-plaquette interactions. However, taking into account the inter-plaquette interactions, the value of \bar{p}^2 reduces from its perfect plaquette ordering amplitude, i.e. $\bar{p}^2 \lesssim 1$, giving rise to a non-zero occupation of other excited bosons, which defines an effective theory for the interacting model (see Eq. 8). To preserve the Hilbert space, we impose the constraint of unit boson occupation for each isolated plaquette, i.e.

$$N\bar{p}^2 + \sum_{I,u=2}^{16} b_{I,u}^\dagger b_{I,u} = N, \quad (6)$$

where N is the total number of shaded uncrossed squares in Fig. 1-(b).

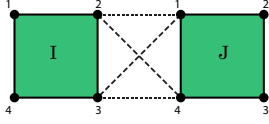


FIG. 4. The interaction between two ‘nearest-neighbor’ plaquettes, I and J . The dotted and dashed lines are J_1 and J_2 couplings, respectively.

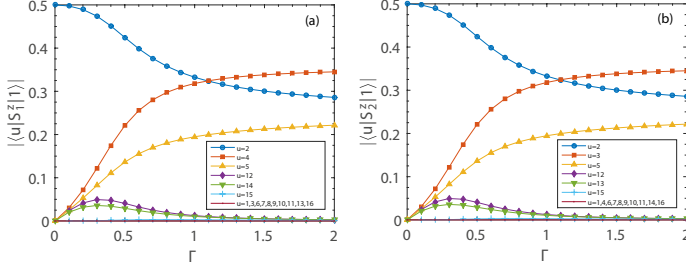


FIG. 5. (color online) Transition amplitudes versus magnetic field between the ground state ($|1\rangle$) and sixteen eigenstates ($|u\rangle$, $u = 1, 2, 3, \dots, 16$) of a plaquette. (a) $|\langle u|S_1^z|1\rangle|$ that is equal to $|\langle u|S_3^z|1\rangle|$. (b) $|\langle u|S_2^z|1\rangle|$, which is equal to $|\langle u|S_4^z|1\rangle|$.

The inter-plaquette interaction between two plaquettes which is shown by Ising terms on dotted and dashed lines of Fig. 4, is called H_{IJ} (details are given in Appendix 1). The state of two nearest neighbor plaquettes I and J in the absence of interactions, is given by $|I_u J_v\rangle$, indicating that the plaquette- I is in the $|u\rangle$ state and plaquette- J in $|v\rangle$. The inter-plaquette interactions are considered in terms of the matrix elements of H_{IJ} between two product states, i.e. $\langle I_u J_v | H_{IJ} | I_s J_t \rangle$. However, because of the Bose-condensation assumption of the ground state background, all other excited bosons will be present in very dilute concentrations. Thus interactions between such dilute bosons are unlikely and we only consider transitions between $u = 1$ groundstate-bosons of each plaquette and the other excited bosons, i.e. we do not consider the matrix elements between excited bosons themselves. In other words, either $|u\rangle$ or $|s\rangle$ for plaquette- I and either $|v\rangle$ or $|t\rangle$ for plaquette- J are necessarily in the state $|1\rangle$. Hence, only terms proportional to \bar{p}^2 participate in the effective Hamiltonian, resulting in a quadratic bosonic form.

The matrix element $\langle I_u J_v | H_{IJ} | I_s J_t \rangle$ is proportional to the transition amplitudes of two S^z operators

$$\langle I_u J_v | H_{IJ} | I_s J_t \rangle \sim \sum_{\{i,j\}} \langle u | S_{i,I}^z | 1 \rangle \times \langle v | S_{j,J}^z | 1 \rangle, \quad (7)$$

where $\{i, j\}$ represents the interaction terms between two adjacent plaquettes (see Fig. 4). We have plotted the transition amplitudes in Fig. 5. It shows that transitions to only eight excited bosonic states are non zero with more significant magnitudes for $u = 2, 3, 4, 5$ (see also Table. I in Appendix 1). Hence, we consider only the first four excited states of each plaquette that contribute in effective Hamiltonian. However, for low transverse fields $\Gamma \lesssim 0.6$, the transition to the first

excited state ($u = 2$) has a dominant role among the four mentioned excited states. Therefore, for low transverse fields in which we obtain an emergent RPS phase, we can reduce the number ‘four’ of excited bosons to only ‘one’ boson (the first excited state of a plaquette). We use this simplified version of our approach in the appendices to obtain the groundstate energy, correlations and order parameters, analytically. However, the whole results of this paper are based on an effective Hamiltonian with four excited bosonic states, described below.

C. Effective Hamiltonian

Finally, taking into account the inter-plaquette interactions, the effective Hamiltonian of the system in the quadratic bosonic form, accompanied by the unit boson occupancy constraint via chemical potential μ , reads as:

$$\begin{aligned} \mathcal{H} = & \sum_I \epsilon_1 \bar{p}^2 + \sum_I \sum_u \epsilon_u b_{I,u}^\dagger b_{I,u} \\ & - \mu \left[N \bar{p}^2 + \sum_{I,u} b_{I,u}^\dagger b_{I,u} - N \right] \\ & + \bar{p}^2 \sum_{\langle IJ \rangle} \sum_{u,v} \left[\langle uv | H_{IJ} | 11 \rangle b_{I,u}^\dagger b_{J,v}^\dagger \right. \\ & \left. + \langle u1 | H_{IJ} | 1v \rangle b_{I,u}^\dagger b_{J,v} + H.c. \right], \quad (8) \end{aligned}$$

where u and v run over the four dominant excited bosonic states of the nearest neighbor plaquettes I and J , respectively. It should be noticed that the Z_2 symmetry of the original Hamiltonian, Eq. 1, is respected in the effective Hamiltonian. This is a consequence of the eigenstates of Eq. 2 that preserve the Z_2 symmetry and, thus, all of the bosonic states participating in the effective Hamiltonian keep this symmetry. The Hamiltonian is written in the momentum space and within a paraunitary Bogoliubov transformation⁴⁰ we arrive at the following diagonal form (see Appendix 1 for details),

$$\begin{aligned} \mathcal{H} = & N\mu + N\bar{p}^2(\epsilon_1 - \mu) - \frac{1}{2}N \sum_u (\epsilon_u - \mu) \\ & + \sum_{\mathbf{k}} \sum_{\nu=1}^4 \left(\frac{1}{2} + \gamma_{\mathbf{k},\nu}^\dagger \gamma_{\mathbf{k},\nu} \right) \omega_{\mathbf{k},\nu}(\mu, \bar{p}), \quad (9) \end{aligned}$$

where \mathbf{k} sums over the first Brillouin zone of a square lattice constructed from the centers of the shaded plaquettes of Fig. 1-(b), $\omega_{\mathbf{k},\nu}$ defines the spectrum of quasi-particles of the interacting model and $\gamma_{\mathbf{k},\nu}^\dagger$ is the corresponding bosonic creation operator. The constant term in Eq. 9 represents the ground state energy of the plaquette-ordered background, which is corrected due to the interaction between plaquettes and takes into account the zero point quantum fluctuations of plaquette type. The two parameters \bar{p} and μ are determined

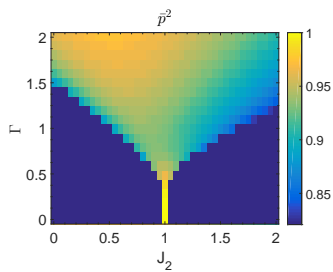


FIG. 6. (color online) The density plot of \bar{p}^2 , the probability of Bose-condensation of $u=1$ -bosons on the plaquette background, as a function of J_2 and Γ . The plaquette order is strong in the bright region, while we do not get a consistent solution of Eqs. 10, 11 for dark blue regions, implying Néel and collinear states.

self-consistently within the following two equations

$$\frac{\partial \langle \mathcal{H} \rangle}{\partial \mu} = 0, \quad (10)$$

$$\frac{\partial \langle \mathcal{H} \rangle}{\partial \bar{p}} = 0. \quad (11)$$

The unit boson occupancy constraint is satisfied by Eq. 10 and the ground state energy is minimized with respect to variational parameter \bar{p} in Eq. 11.

III. RESULTS

First, we examine the validity region of POA, where the Bose-condensation of $u=1$ -bosons has to appear. This is justified as far as \bar{p}^2 is close to unity, i.e. the strong plaquette order. The density plot of \bar{p}^2 versus J_2 and Γ is shown in Fig. 6. In the intermediate bright region of Fig. 6, we find $\bar{p}^2 \gtrsim 0.85$, which states that POA works very well. However, there exists dark blue area (in Fig. 6) in which we can not find a simultaneous solution of Eqs. 10, 11. It shows that the unit boson occupancy constraint is not fulfilled in the dark blue regions. This seems to be a rational consequence of comparing the ground state energy of the primary plaquette background with those of the classical Néel or collinear backgrounds (see Fig. 3). Specially, for the low field and weakly frustrated regions we get higher ground state energy for the plaquette background than the other classical backgrounds. This is also a result of gap vanishing by approaching the dark blue area, where the elementary excitations of the model become gapless leading to a different type of ordering with different background condensation. Hence, approaching the dark blue region, the hypothesis of Bose-condensation of $u=1$ -bosons can not be justified anymore. However, we observe evidences for the existence of Néel and collinear phases by reaching the gapless critical border, which will be described in the following.

As a first indication, we evaluate the minimum of the excitation spectrum $\omega_{\mathbf{k},\nu}$, which defines the energy gap of our model. It is plotted in Fig. 7-(a) versus J_2 for different values of the transverse field Γ . We observe that at a fixed value of Γ , the energy gap vanishes at two critical couplings of J_2 ,

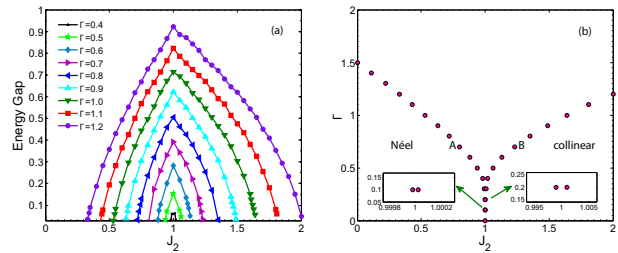


FIG. 7. ((color online) (a) The energy gap versus J_2 for different values of transverse field (Γ). The gap is finite in the intermediate region, while it vanishes at two critical values of J_2 . (b) The location of critical points, which corresponds to the vanishing of energy gap in the phase diagram. The insets indicate an opening of a narrow region around $J_2 = J_1$, where the gap is still finite for low fields.

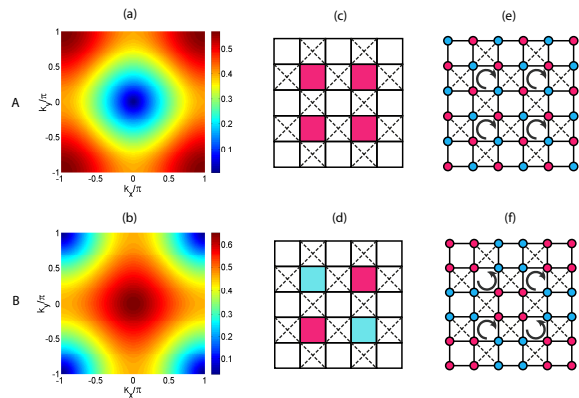


FIG. 8. (color online) Up and Down rows correspond respectively to the critical points A ($J_2 = 0.80$) and B ($J_2 = 1.23$) for $\Gamma = 0.7$. (a) and (b): Density plots of the lowest band of bosonic excitation spectrum. The excitation energy vanishes at $(k_x = 0, k_y = 0)$ for point A and $(\pm\pi, \pm\pi)$ for point B. (c) and (d): the type of plaquette ordering of the groundstate. A symmetric covering for point A and a staggered one for point B. (e) and (f): The classical representations for the Néel and collinear states, which can be mapped to the middle pictures (c) and (d) with plaquette-type orderings. Clockwise and counter-clockwise arrows represent the kind of arrangement of up and down (red and blue) spins in adjacent plaquettes.

which corresponds to the locations of quantum phase transitions. The quantum critical points in the $\Gamma - J_2$ plane are shown in Fig. 7-(b), which displays the phase diagram of our model representing two critical boundaries.

One of the key features of the plaquette operator approach, compared to LSWT³¹, is to lift the exponential degeneracy of the classical collinear phase toward a unique quantum collinear state. Of course, it leaves a fourfold degeneracy, two of them coming from the Z_2 symmetry and the other two from the translational symmetry. In order to demonstrate this assertion we have studied the lowest band of excitation spectrum $\omega_{\nu,\mathbf{k}}$ for $\Gamma = 0.7$ and at the two critical couplings $J_2 = 0.80$ and $J_2 = 1.23$, corresponding to the gapless points A and B, shown in Fig. 7-(b). The density plot of the lowest band of excitation spectrum is shown in Fig. 8-(a) and (b) corresponding to the points A and B, respectively.

The density plots show that the gapless points occur at different k -vectors for A and B. As we see, the excitation spectrum reaches a minimum at the ferromagnetic wave vector ($k_x = 0, k_y = 0$) for A (Fig. 8-(a)), while it becomes minimum at the anti-ferromagnetic wave vector ($k_x = \pm\pi, k_y = \pm\pi$) for B (Fig. 8-(b)). It reveals the construction of different orderings at these two critical points. The wave vector (k_x, k_y) corresponds to the type of plaquette ordering of the lattice⁴¹. A minimum at the ferromagnetic wave vector ($k_x = 0, k_y = 0$) indicates a ferromagnetic tiling of resonating plaquettes, shown in Fig. 8-(c) which can be equivalent to a Néel configuration of the whole lattice shown in Fig. 8-(e). In fact, four shaded plaquettes in Fig. 8-(c) are in the same resonating state, similar to the same orientation of spins on neighboring plaquettes of a Néel state of Fig. 8-(e). Thus, the critical point A evidently expresses a transition to a Néel phase. On the other side, a minimum at ($k_x = \pm\pi, k_y = \pm\pi$) corresponds to a staggered (anti-ferromagnetic) plaquette covering of the lattice at point B which is equivalent to a specific collinear order for the whole lattice. In fact, the staggered ordering of plaquettes in Fig. 8-(d) acts like the opposite orientation of spins in the adjacent plaquettes of a particular collinear state shown in Fig. 8-(f). Hence, the critical point B corresponds to a quantum phase transition to a unique collinear state. Interestingly, we conclude that plaquette-type excitations of POA are proper candidates to lift the extensive degeneracy of a classical groundstate, compared to the single-spin-flip ones of LSWT³¹.

The above arguments are true for the whole transition points of Fig.7-(b), i.e. the gap vanishes at ($k_x = 0, k_y = 0$) for the critical line in $J_2 < 1$ and it vanishes at ($k_x = \pm\pi, k_y = \pm\pi$) for the critical line in $J_2 > 1$. More justification for the Néel and collinear orders is given by the nearest neighbor (NN) and next-nearest neighbor (NNN) correlation functions. As shown in Fig. 15 (of Appendix 2), the NN correlation $\langle S_i^z S_j^z \rangle_{\langle i,j \rangle}$ is always negative at both critical points A and B, while the NNN correlation $\langle S_i^z S_j^z \rangle_{\langle\langle i,j \rangle\rangle}$ is positive at point A and becomes negative for B, confirming the Néel and collinear orders, respectively. Accordingly, the two critical lines of the phase diagram correspond to a transition to the Néel phase for $J_2 < 1$ and to the collinear phase for $J_2 > 1$.

Having determined the transition lines to the Néel and collinear phases, we now study the bright intermediate region of Fig. 6, in which we obtain the condensation of $u=1$ -bosons ($\bar{p}^2 \gtrsim 0.85$). This area covers the regions, where LSWT breaks down in the vicinity of classical phase boundaries (see Fig.9 of Ref.³¹). Thus, we expect that POA improves the phase diagram of the model, via plaquette-type quantum fluctuations. We calculate the transverse magnetization $\langle S_x \rangle$, which is shown as a density plot in Fig. 9-(a) (for details see Appendix 3). The value of transverse magnetization is high enough for $\Gamma \gtrsim 0.3$, imitating a quantum paramagnet (polarized) phase. In fact, in the quantum paramagnet phase, $\langle S_x \rangle$ is less than its maximal classical value of 0.5 due to strong quantum fluctuations. Thus, we conclude that POA can reproduce the polarized phase of high fields in such a way that all plaquettes are in their polarized states, restoring the translational symmetry of the lattice.

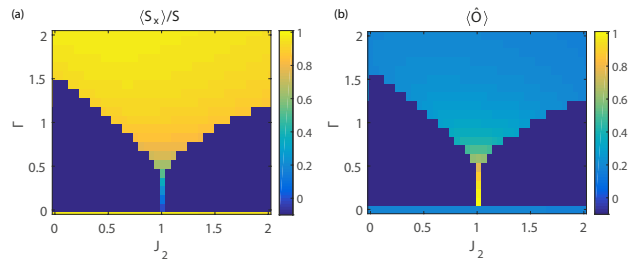


FIG. 9. (color online) (a) The density plot of transverse magnetization $\langle S_x \rangle / S$ versus J_2 and Γ . (b) The density plot of plaquette order parameter $\langle \hat{O} \rangle$ versus J_2 and Γ . The dark blue part is the region where the constraint of one boson per plaquette is not satisfied and contains no data.

On the other hand, for low transverse fields $\Gamma \lesssim 0.3$, the value of transverse magnetization $\langle S_x \rangle$ deviates dramatically from its saturated value, revealing the onset of a new phase. In contrast to the result of LSWT³¹, the emergent new phase is neither a Néel nor a collinear state, which can be confirmed via energy considerations. The ground state energy per spin (GSE) is plotted in Fig. 10 versus J_2 for two different values of transverse field $\Gamma = 0.3, 0.7$.

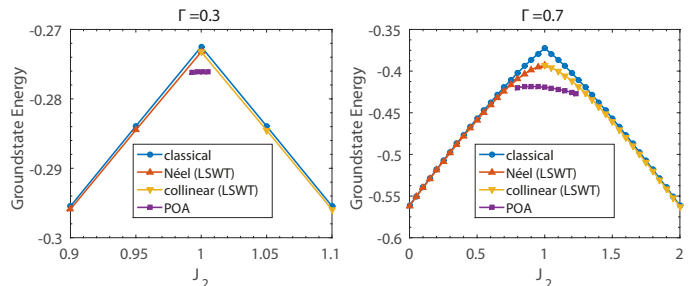


FIG. 10. (color online) The groundstate energy per spin (in units of J_1) versus J_2 for $\Gamma = 0.3$ and 0.7 . The upper blue line (\bullet) shows the result of classical ($S \rightarrow \infty$) approximation, the orange (\blacktriangle) and yellow (\blacktriangledown) lines represent the results of LSWT based on the Néel and collinear backgrounds, respectively (Ref.³¹) and the lower purple line (\blacksquare) demonstrates the result of POA of the present work.

Obviously, for both transverse fields and in the intermediate region around $J_2 = J_1$, the GSE of POA is lower than the corresponding classical and LSWT ones. It justifies strongly that POA gives a more precise representation of the groundstate for the bright region of Fig. 6. Now in order to understand the nature of phase for $\Gamma \lesssim 0.3$, we define the resonating plaquette operator

$$\hat{O} = |\varphi\rangle\langle\bar{\varphi}| + |\bar{\varphi}\rangle\langle\varphi|, \quad (12)$$

in which $|\varphi\rangle = |\uparrow\downarrow\uparrow\downarrow\rangle$ and $|\bar{\varphi}\rangle = |\downarrow\uparrow\downarrow\uparrow\rangle$ are two possible Néel configurations of a single plaquette (\uparrow and \downarrow represent the two eigenstates of S^z operator at the four corners of a plaquette). In fact, \hat{O} defines a measure of resonating magnitude between $|\varphi\rangle$ and $|\bar{\varphi}\rangle$ on a plaquette. Hence, the expectation value of \hat{O} is close to one for a resonating plaquette solid state

(RPS), which has no magnetic order in z-direction. Fig. 9-(b) shows the density plot of $\langle \hat{O} \rangle$, which is an outcome of POA (for details see Appendix 3). It is evident that for a narrow region around $J_2 = J_1$ and $\Gamma \lesssim 0.3$, the value of $\langle \hat{O} \rangle$ is very close to unity. However, there exist a small amount of field induced magnetization for this region (see Fig. 9-(a)) that propose to call it a canted RPS phase. It implies a resonating plaquette-type ordering in addition to a small inclination along the transverse field. A schematic representation of this phase is shown in Fig. 1-(b). The emergent RPS phase breaks translational symmetry of the lattice and is two-fold degenerate. Therefore, the plaquette-type quantum fluctuations of POA are able to lift the extensive degeneracy of the square ice, leading to an *order by disorder*.

Finally, according to above arguments, the phase diagram of TFIM on the checkerboard lattice, obtained from POA, is sketched in Fig. 11. In the limit of $J_2 = 0$, in which the system reduces to TFIM on the square lattice, the gap vanishes at $\Gamma = 1.50$, which corresponds to the quantum phase transition from quantum paramagnet to the Néel phase. It is in very good agreement with the results of density matrix renormalization group⁴², extended coupled cluster method⁴³ and quantum Monte-Carlo simulation⁴⁴, which report the critical point of the square lattice TFIM at $\Gamma = 1.50$ ⁴³ and $\Gamma = 1.52$ ^{42,44}. This is a success of POA compared with LSWT³¹, which gives $\Gamma_c^{(LSWT)} = 2.0$ for $J_2 = 0$. Thus, we anticipate that the whole critical lines shown in Fig. 11 give an accurate phase diagram of the model. Moreover, the non-monotonic behavior of the ground state energy in LSWT leads to an inconsistency of the sign of NNN correlation function close to the critical boundaries³¹. In addition, we obtain an RPS state at low fields in a narrow region around $J_2 = J_1$, which has not been observed via LSWT. The existence of a canted RPS phase confirms the results of Monte-Carlo studies of Refs.²⁹ and ⁴⁵, as well as the result of quantum dimer model²⁸.

As we mentioned earlier, the single boson occupancy constraint (Eq. 10) is not satisfied in the area denoted by the Néel and collinear states in the phase diagram. Hence, we are not able to study the nature of phase transitions to these magnetically ordered phases, in terms of antiferromagnetic order parameter. Nevertheless, we predict that transition from quantum paramagnet to either Néel or collinear phases should be of a continuous second order type, similar to the transition at $\Gamma = 1.5$ for $J_2 = 0$ limit⁴²⁻⁴⁴.

Now, let us investigate the transition between RPS and quantum paramagnet phase at $J_2 = J_1$. In this respect, we calculate some properties of the model at the isotropic case $J_2 = J_1$ versus transverse field Γ , shown in Fig. 12. The plaquette order parameter $\langle \hat{O} \rangle$ is shown in Fig. 12-(a), which indicates a deep decreasing from unity when increasing the transverse field Γ , although it does not reach zero because of strong quantum fluctuations. The reduction of plaquette order parameter is accompanied with a sharp increment of the transverse magnetization $\langle \hat{S}_x \rangle$ toward its saturated value, shown in Fig. 12-(b). Thus, there should be a continuous phase transition between RPS state at low fields and the quantum paramagnet phase for high fields. This is supported by the broken

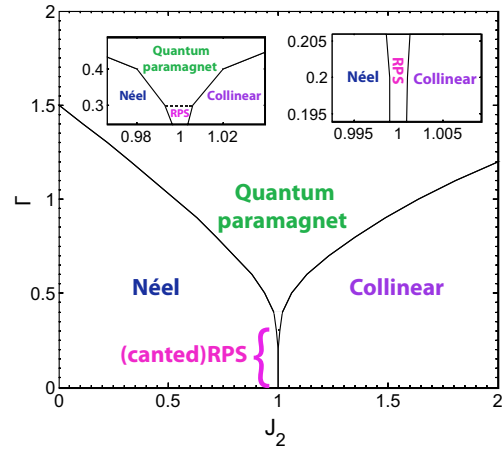


FIG. 11. (color online) Phase diagram of S=1/2 TFIM on the checkerboard lattice within the plaquette operator approach. The phase boundaries to the Néel and collinear ordered states are denoted by black-solid lines. Both insets show the narrow (canted) RPS phase, which fills the space between the Néel and collinear phases around $J_2 = J_1$ for $\Gamma \lesssim 0.3$.

translational symmetry of the RPS phase compared with the translational invariance of quantum paramagnet. Nevertheless, the quasi-particle excitation gap, shown in Fig. 12-(c), vanishes only at $\Gamma = 0$, which does not show a quantum phase transition at finite- Γ and $J_2 = J_1$. However, the non-linear trend of energy gap for $\Gamma \lesssim 0.3$ (see the inset of Fig. 12-(c)) is changed to the linear behavior for the $\Gamma \gtrsim 0.3$, which is the property of a quantum paramagnet. On the other hand, the first derivative of transverse magnetization, i.e. the susceptibility, demonstrates a peak at $\Gamma \simeq 0.3$ shown in Fig. 12-(d). To justify our results, we have employed the Lanczos exact-diagonalization method to calculate the ground state of our model. We consider a 16-sites (4×4) lattice with periodic boundary condition. The results of magnetization ($\langle \hat{S}_x \rangle$) and its corresponding susceptibility have been shown in Fig.12 (b),(d) that show a fairly good agreement.

Accordingly, we deduce that a quantum phase transition should split the RPS and quantum paramagnet phases, although our approach does not show a zero gap mode, which should be checked precisely, using further numerical techniques. A similar situation has been observed in the POA of the frustrated honeycomb antiferromagnet, where the gap of POA does not vanish³³ at the expected transition points between a plaquette-RVB phase and Néel or dimer phases; However, numerical DMRG computations¹¹ justifies the closure of gap at the mentioned transition points.

IV. SUMMARY AND DISCUSSIONS

We have studied the zero-temperature phase diagram of the transverse field Ising model on the checkerboard lattice, with nearest and next-nearest neighbor couplings J_1 and J_2 , respectively. This model is a frustrated magnetic system, which

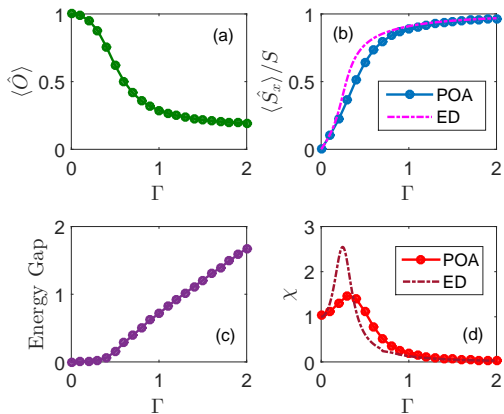


FIG. 12. (color online) Features of the isotropic case $J_2 = J_1$ versus Γ . (a) plaquette order parameter $\langle \hat{O} \rangle$, (b) transverse magnetization $\langle \hat{S}_x \rangle / S$ obtained from POA, which is compared with the result of a 16-sites Lanczos-ED calculation, (c) the energy gap which shows a linear behavior for $\Gamma \gtrsim 0.3$, indicating a quantum paramagnet phase and (d) the first derivative of transverse magnetization with respect to Γ (χ), with a peak at $\Gamma \simeq 0.3$ implying a phase transition. The data obtained from 16-sites Lanczos-ED calculation with a peak at $\Gamma \simeq 0.24$ is also shown for comparison.

has an extensive degenerate classical groundstate for $J_2 \geq J_1$. The LSWT analysis of the model fails to lift the classical degeneracy of the collinear phase; moreover, the corresponding phase diagram show some instabilities near the classical boundaries³¹. This implies that the harmonic fluctuations, which come from the single-spin-flip excitations of LSWT, can not give the true quantum fluctuations of the system, specially close to the phase boundaries and highly frustrated region $J_2 = J_1$. Here, we have applied a plaquette operator approach, which is based on the bosonization of the model, in which a boson is associated to each plaquette eigenstate. A Bose-condensation of the plaquette ground state is assumed, which survives as far as the excitation energy gap is non-zero. The effective Hamiltonian, Eq. 9, which takes into account the interaction between plaquettes, describes the ground state phase diagram of the model. We would like to mention that the harmonic fluctuations of the effective Hamiltonian are essentially an-harmonic fluctuations of the original spin model that are proper quantum fluctuations as the elementary excitations of the model.

According to Fig. 3, POA is a high-field approach, which also gives reliable results for the low-fields in the highly frustrated region, where an emergent RPS phase shows up. The phase diagram, Fig. 11, consists of four phases, quantum paramagnet phase, Néel phase, collinear ordered phase and an RPS phase for low fields $\Gamma \lesssim 0.3$, a narrow region around $J_2 = J_1$. In fact, the exponential degeneracy of the classical groundstate at $J_2 = J_1$ (square ice) is lifted toward a unique quantum RPS state that breaks translational symmetry of the lattice leaving two-fold degeneracy. It is a manifestaion of order-by-disorder that is induced by quantum fluctuations. Disclosing the RPS phase is consistent with the results of the

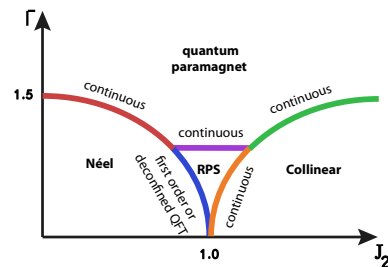


FIG. 13. (color online) A schematic picture to specify the type of transitions on the phase diagram (Fig. 11). The red and green lines correspond to continuous quantum phase transition (QPT) from quantum paramagnet to the Néel and collinear phases, respectively. The purple line shows the continuous transition from quantum paramagnet to RPS phase. The blue and orange lines are related to transitions from RPS phase to the Néel and collinear phases, respectively. The former should be either a first order type or a deconfined QPT, but the latter is a continuous QPT.

quantum dimer model²⁸ as an effective Hamiltonian on the degenerate Hilbert space at $J_2 = J_1$, which gives a plaquette ordered state for the zero chemical potential. On the other hand, the boundaries to the Néel and collinear phases, corresponding to the vanishing of quasi-particle excitation gap is determined consistently via POA, in contrast to LSWT. In addition, one of the smart features of POA is that the formation of Néel and collinear phases are realized according to the type of plaquette ordering at the transition points, which also reveals lifting the exponential degeneracy of the classical collinear phase toward a unique one. Accordingly, the Néel and collinear phases are separated by a quantum paramagnet for the high-field region and by an RPS phase for the low-field region, where the critical boundaries merge only at the zero field $\Gamma = 0$. Our POA results for $J_2 = 0$, manifest a transition from the Néel to quantum paramagnet at $\Gamma = 1.50$, which is fully consistent with the result of TFIM on the square lattice with a second order phase transition at the critical field $\Gamma = 1.50$ ⁴³ or $\Gamma = 1.52$ ^{42,44}. It suggests that the phase transition from quantum paramagnet to the Néel or collinear phases should be of a continuous second order type. This continuous phase transition persists for low fields between RPS and collinear phases. In fact, although both the collinear and RPS phases break translational symmetry, the Z_2 symmetry is only broken at the collinear phase, which suggests the transition to be of continuous type. However, the transition from RPS to the Néel phase at low fields should be a first order or a deconfined quantum phase transition⁴⁶, as they break different symmetries (Z_2 symmetry against translational symmetry). Finally, we anticipate a continuous phase transition from RPS to quantum paramagnet phase (see Fig. 13).

A recently Monte-Carlo study of the TFIM on the isotropic $J_2 = J_1$ checkerboard lattice⁴⁵, reports an RPS state, via an extrapolation to zero-temperature, that persists up to $\Gamma \simeq 0.13$ and a canted Néel state for $0.13 \lesssim \Gamma \lesssim 0.28$ and finally a quantum paramagnet phase for higher fields ($\Gamma \gtrsim 0.28$). However, the presence of such a Néel phase is a very delicate issue, which requires more justifications. According to Ref.⁴⁵,

the Néel phase does not come from direct simulation on the original Hamiltonian, rather it is an outcome of the simulation on the fourth order effective Hamiltonian that can be constructed from the extensive degenerate manifold at $J_2 = J_1$. Moreover, the extrapolated ($N \rightarrow \infty$) staggered magnetization is obtained to be $m_s \sim 10^{-2}$, which is very small. On the other hand, we do not observe a signature for a Néel phase at $J_2 = J_1$, which convinces us that the phase diagram at the highly frustrated point $J_2 = J_1$ consists only of an RPS and a quantum paramagnet. Hence, we predict that a quantum phase transition should occur between the RPS and quantum paramagnet phases, although our approach does not show a zero gap mode, which can only be checked using precise numerical techniques.

V. ACKNOWLEDGMENT

The authors would like to thank R. Moessner, I. Rousochatzakis and P. Thalmeier for fruitful discussions and comments. This work was supported in part by the Office of Vice-President for Research of Sharif University of Technology. A. L. gratefully acknowledges the Alexander von Humboldt Foundation for financial support.

1. Ground-state energy for the RPS phase

The interaction Hamiltonian between the isolated plaquette I and its four nearest-neighbor plaquettes reads as (see Fig. 14):

$$\begin{aligned}
H_{I\delta_1} &= J_1 s_{2(I)}^z s_{1(I+\delta_1)}^z + J_1 s_{3(I)}^z s_{4(I+\delta_1)}^z \\
&\quad + J_2 s_{2(I)}^z s_{4(I+\delta_1)}^z + J_2 s_{3(I)}^z s_{1(I+\delta_1)}^z, \\
H_{I\delta_2} &= J_1 s_{1(I)}^z s_{2(I+\delta_2)}^z + J_1 s_{4(I)}^z s_{3(I+\delta_2)}^z \\
&\quad + J_2 s_{4(I)}^z s_{2(I+\delta_2)}^z + J_2 s_{1(I)}^z s_{3(I+\delta_2)}^z, \\
H_{I\delta_3} &= J_1 s_{1(I)}^z s_{4(I+\delta_3)}^z + J_1 s_{2(I)}^z s_{3(I+\delta_3)}^z \\
&\quad + J_2 s_{1(I)}^z s_{3(I+\delta_3)}^z + J_2 s_{2(I)}^z s_{4(I+\delta_3)}^z, \\
H_{I\delta_4} &= J_1 s_{4(I)}^z s_{1(I+\delta_4)}^z + J_1 s_{3(I)}^z s_{2(I+\delta_4)}^z \\
&\quad + J_2 s_{3(I)}^z s_{1(I+\delta_4)}^z + J_2 s_{4(I)}^z s_{2(I+\delta_4)}^z.
\end{aligned} \tag{Appendix 13}$$

Accordingly, we obtain an effective Hamiltonian for the plaquette-ordered background of POA :

$$\begin{aligned}
\mathcal{H} &= N\bar{p}^2(\epsilon_1 - \mu) + N\mu + \sum_I \sum_u (\epsilon_u - \mu) b_{I,u}^\dagger b_{I,u} \\
&\quad + \frac{1}{2}\bar{p}^2 \sum_I \sum_{\delta=\delta_1}^{\delta_4} \sum_{u,v} [\langle uv|H_{I\delta}|11\rangle b_{I,u}^\dagger b_{I+\delta,v}^\dagger \\
&\quad + \langle u1|H_{I\delta}|1v\rangle b_{I,u}^\dagger b_{I+\delta,v} + H.C.],
\end{aligned} \tag{Appendix 14}$$

where index I runs over all shaded plaquettes and δ sums over the four nearest neighbors of each plaquette as shown in Fig. 14.

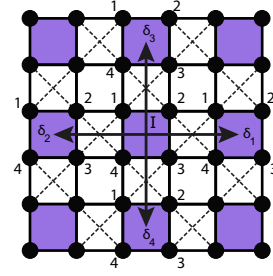


FIG. 14. The checkerboard lattice: each isolated plaquette I interacts with four nearest-neighbor ones. The solid and dashed lines are J_1 and J_2 bonds, respectively.

A transition-amplitude like $\langle uv|J_1 s_{2(I)}^z s_{1(I+\delta_1)}^z |11\rangle$ can be reduced to a product of matrix elements of the single-plaquette operators as:

$$\langle uv|J_1 s_{2(I)}^z s_{1(I+\delta_1)}^z |11\rangle = J_1 \langle u|s_{2(I)}^z|1\rangle \times \langle v|s_{1(I+\delta_1)}^z|1\rangle. \tag{Appendix 15}$$

We have plotted the transition matrix elements versus magnetic field in Fig. 5, however, we summarize few cases in the following table to have an impression of the values. Table. I shows the matrix elements $\langle u|s_\alpha^z|1\rangle$ for three values of transverse field $\Gamma = 1.0, 0.5, 0.1$ in which u runs over sixteen eigenstates of a single plaquette and $\alpha = 1, 2, 3, 4$ represents the four spin-z operators at the four corners of a plaquette. It reveals that transition from groundstate $|1\rangle$ to eight eigenstates $|u\rangle$ of a single plaquette is non-zero, within which only four of them have a significant value, corresponding to $u = 2, 3, 4, 5$. However, we observe that for low values of transverse field Γ , the transition to the first excited state $u = 2$ is more dominant. Therefore, for low transverse fields in which we obtain an emergent RPS phase, we can reduce the number of excited bosons that contribute to the effective Hamiltonian, to only 'one' boson i.e. the first excited $u = 2$ state of each plaquette. Accordingly, in the following we only consider the $u = 2$ state as an excited boson, participating in the effective Hamiltonian of Eq. Appendix 14. We calculate analytically the ground-state energy of RPS phase, as well as spin-spin correlation functions and order parameters via this simplified version of POA.

In order to diagonalize the effective Hamiltonian, we first rewrite it in the momentum space representation using the following transformations

$$b_{\mathbf{k},u} = \frac{1}{\sqrt{N}} \sum_{\mathbf{r}_I} b_{I,u} e^{-i\mathbf{k}\cdot\mathbf{r}_I}, \quad H_{\mathbf{k}} = \sum_{\mathbf{k}} \mathbf{M}_{\mathbf{k}} \tag{Appendix 16}$$

which gives

$$\begin{aligned}
\mathcal{H} &= N\bar{p}^2(\epsilon_1 - \mu) + N\mu - \frac{1}{2}N(\epsilon_2 - \mu) \\
&\quad + \frac{1}{2} \sum_{\mathbf{k}} (b_{\mathbf{k},2}^\dagger, b_{-\mathbf{k},2}) \mathbf{M}_{\mathbf{k}} (b_{\mathbf{k},2}, b_{-\mathbf{k},2}^\dagger)
\end{aligned} \tag{Appendix 17}$$

where, the groundstate energy of a plaquette (ϵ_1), and the first

TABLE I. The values of transition amplitude $\langle u|s_\alpha^z|1\rangle$, from the groundstate of a single plaquette to its sixteen eigenstates, for different values of transverse field Γ .

u	1	2	3	4	5	6	7	8	9	10	11	12	13	14	15	16
$\Gamma = 1.0$																
$\langle u s_1^z 1\rangle$	0	-0.332	0	-0.318	-0.194	0	0	0	0	0.012	0	0	-0.010	-0.002	0	0
$\langle u s_2^z 1\rangle$	0	0.332	-0.318	0	-0.194	0	0	0	0	-0.012	0	-0.010	0	-0.002	0	0
$\langle u s_3^z 1\rangle$	0	-0.332	0	0.318	-0.194	0	0	0	0	0.012	0	0	0.010	-0.002	0	0
$\langle u s_4^z 1\rangle$	0	0.332	0.318	0	-0.194	0	0	0	0	-0.012	0	0.010	0	-0.002	0	0
$\Gamma = 0.5$																
$\langle u s_1^z 1\rangle$	0	-0.424	0	-0.220	-0.136	0	0	0	0	0.040	0	0	-0.029	-0.002	0	0
$\langle u s_2^z 1\rangle$	0	0.424	-0.220	0	-0.136	0	0	0	0	-0.040	0	-0.029	0	-0.002	0	0
$\langle u s_3^z 1\rangle$	0	-0.424	0	0.220	-0.136	0	0	0	0	0.040	0	0	0.029	-0.002	0	0
$\langle u s_4^z 1\rangle$	0	0.424	0.220	0	-0.136	0	0	0	0	-0.040	0	0.029	0	-0.002	0	0
$\Gamma = 0.1$																
$\langle u s_1^z 1\rangle$	0	-0.497	0	-0.030	-0.025	0	0	0	0	0.023	0	0	-0.020	-0.000	0	0
$\langle u s_2^z 1\rangle$	0	0.497	-0.030	0	-0.025	0	0	0	0	-0.023	0	-0.020	0	-0.000	0	0
$\langle u s_3^z 1\rangle$	0	-0.497	0	0.030	-0.025	0	0	0	0	0.023	0	0	0.020	-0.000	0	0
$\langle u s_4^z 1\rangle$	0	0.497	0.030	0	-0.025	0	0	0	0	-0.023	0	0.020	0	-0.000	0	0

excited one (ϵ_2) have the following expressions

$$\epsilon_1 = -\frac{\sqrt{1+4\Gamma^2} + \sqrt{1+16\Gamma^4}}{\sqrt{2}}, \epsilon_2 = \frac{1}{2}(-1 - \sqrt{1+4\Gamma^2}). \quad (\text{Appendix 18})$$

The elements of $M_{\mathbf{k}}$ is as follows,

$$\begin{aligned} M_{11} &= M_{22} = (\epsilon_2 - \mu) + 2f\bar{p}^2(\cos k_x + \cos k_y), \\ M_{12} &= M_{21} = 2f\bar{p}^2(\cos k_x - \cos k_y), \end{aligned} \quad (\text{Appendix 19})$$

in which f is a function of Γ and J_2 (which has not been shown here due to its long expression). The Hamiltonian Eq. Appendix 17 is diagonalized via a paraunitary Bogoliubov transformation⁴⁰ as,

$$\mathcal{H} = N\bar{p}^2(\epsilon_1 - \mu) + N\mu - \frac{1}{2}N(\epsilon_2 - \mu) + \sum_{\mathbf{k}} \left(\frac{1}{2} + \gamma_{\mathbf{k}}^\dagger \gamma_{\mathbf{k}} \right) \omega_{\mathbf{k}}, \quad (\text{Appendix 20})$$

where the eigenmodes read as

$$\omega_{\mathbf{k}} = \sqrt{(\epsilon_2 - \mu)(\epsilon_2 - \mu + 4f\bar{p}^2(\cos k_x + \cos k_y))}. \quad (\text{Appendix 21})$$

Finally, the groundstate energy of the RPS phase becomes

$$E_{RPS} = N\bar{p}^2(\epsilon_1 - \mu) + N\mu - \frac{1}{2}N(\epsilon_2 - \mu) + \frac{1}{2} \sum_{\mathbf{k}} \omega_{\mathbf{k}}, \quad (\text{Appendix 22})$$

in which \bar{p} and μ are determined self-consistently using simultaneous numerical solution of the following equations

$$\frac{\partial E_{RPS}}{\partial \mu} = 0, \quad (\text{Appendix 23})$$

$$\frac{\partial E_{RPS}}{\partial \bar{p}} = 0. \quad (\text{Appendix 24})$$

Eq. Appendix 23 satisfies the unit boson occupancy constraint, and Eq. Appendix 24 minimizes the ground state energy with respect to \bar{p} .

2. Nearest and next-nearest neighbor correlation functions

The nearest and next-nearest neighbor correlation functions corresponding to $C^{(1)} = \langle S_i^z S_j^z \rangle_{\langle i,j \rangle} = \partial \langle \mathcal{H} \rangle / \partial J_1$ and $C^{(2)} = \langle S_i^z S_j^z \rangle_{\langle\langle i,j \rangle\rangle} = \partial \langle \mathcal{H} \rangle / \partial J_2$ are plotted in Fig. 15 versus J_2 , at a low transverse field $\Gamma = 0.4$. The plot justifies the change of ordering structure to the Néel and collinear phases, when approaching to the critical points $J_2 \approx 0.99$ and $J_2 \approx 1.01$, respectively. As a matter of fact, it is expected from the classical picture presented in Fig. 1 that the nearest neighbor correlations in a collinear phase is weaker, in strength, than in the Néel phase (the average number of aligned and anti-aligned nearest-neighbor bonds are roughly the same in the collinear order, compared to all anti-aligned nearest-neighbor bonds in the Néel order). This is confirmed evidently in the plot of nearest neighbor correlation of Fig. 15. Moreover, according to the classical picture, the next-nearest neighbor correlations are positive for the Néel order, while they are negative in the collinear order. Therefore, the change

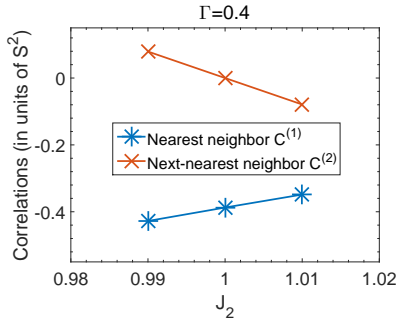


FIG. 15. (color online) The nearest and next-nearest neighbor correlations as a function of J_2 , for a low transverse field $\Gamma = 0.4$. The change of sign at $J_2 = 1$ for the next-nearest neighbor correlation function represents the change of tendency to construct different orderings, i.e. a Néel order for $J_2 \lesssim 0.99$ and a collinear order for $J_2 \gtrsim 1.01$.

of sign in the next-nearest-neighbor correlation at $J_2 = 1$ in Fig. 15 is a signature of entering from the RPS phase to the Néel and collinear phases, at $J_2 \approx 0.99$ and $J_2 \approx 1.01$, respectively.

3. Order Parameters

The expectation values of the order-parameter operators \hat{O} and \hat{S}_x are calculated for the RPS state at low fields, making use of the density matrix formalism. In the simplified one-excited-boson version of POA, the density matrix operator $\hat{\rho}$ of a single plaquette takes the following form

$$\hat{\rho} = \bar{p}^2 |1\rangle\langle 1| + (1 - \bar{p}^2) |2\rangle\langle 2| \quad (\text{Appendix 25})$$

where $|1\rangle$ denotes the groundstate of the single plaquette, $|2\rangle$ is the first excited state, and \bar{p}^2 is the probability of finding the single plaquette in its groundstate.

The expectation values of the plaquette order parameter \hat{O} (which is defined in Eq. 12) and the transverse magnetization are given by the following equations

$$\begin{aligned} \langle \hat{O} \rangle &= Tr(\hat{O}\hat{\rho}) = \bar{p}^2 \langle 1|\hat{O}|1\rangle + (1 - \bar{p}^2) \langle 2|\hat{O}|2\rangle, \\ \langle \hat{S}_x \rangle &= Tr(\hat{S}_x\hat{\rho}) = \bar{p}^2 \langle 1|\hat{S}_x|1\rangle + (1 - \bar{p}^2) \langle 2|\hat{S}_x|2\rangle. \end{aligned} \quad (\text{Appendix 26})$$

Extending the above arguments to the general version of POA (with four excited bosons, contributing to the effective Hamiltonian), we obtain the groundstate energy, the order parameters and other quantities for the whole values of transverse field Γ , as presented in Sec. III.

* marzieh.sadrzadeh@physics.sharif.edu; <http://spin.cscm.ir/>

- ¹ C. Castelnovo, R. Moessner, and S. L. Sondhi, *Nature* **451**, 42 (2008).
- ² P. Anderson, *Materials Research Bulletin* **8**, 153 (1973).
- ³ R. Moessner, S. L. Sondhi, and P. Chandra, *Phys. Rev. Lett.* **84**, 4457 (2000).
- ⁴ R. Moessner and S. L. Sondhi, *Phys. Rev. Lett.* **86**, 1881 (2001).
- ⁵ R. Moessner and S. L. Sondhi, *Phys. Rev. B* **63**, 224401 (2001).
- ⁶ G. Misguich and F. Mila, *Phys. Rev. B* **77**, 134421 (2008).
- ⁷ D. S. Rokhsar and S. A. Kivelson, *Phys. Rev. Lett.* **61**, 2376 (1988).
- ⁸ A. F. Albuquerque, D. Schwandt, B. Hetényi, S. Capponi, M. Mambri, and A. M. Läuchli, *Phys. Rev. B* **84**, 024406 (2011).
- ⁹ H. Mosadeq, F. Shahbazi, and S. A. Jafari, *Journal of Physics: Condensed Matter* **23**, 226006 (2011).
- ¹⁰ Z. Zhu, D. A. Huse, and S. R. White, *Physical Review Letters* **110**, 127205 (2013).
- ¹¹ R. Ganesh, J. van den Brink, and S. Nishimoto, *Phys. Rev. Lett.* **110**, 127203 (2013).
- ¹² M. E. Zhitomirsky and K. Ueda, *Phys. Rev. B* **54**, 9007 (1996).
- ¹³ L. Isaev, G. Ortiz, and J. Dukelsky, *Physical Review B* **79**, 024409 (2009).
- ¹⁴ S. Wenzel, T. Coletta, S. E. Korshunov, and F. Mila, *Phys. Rev. Lett.* **109**, 187202 (2012).
- ¹⁵ R. Doretto, *Physical Review B* **89**, 104415 (2014).
- ¹⁶ S.-S. Gong, W. Zhu, D. Sheng, O. I. Motrunich, and M. P. Fisher, *Physical review letters* **113**, 027201 (2014).
- ¹⁷ H.-C. Jiang, H. Yao, and L. Balents, *Physical Review B* **86**, 024424 (2012).
- ¹⁸ S. E. Palmer and J. T. Chalker, *Phys. Rev. B* **64**, 094412 (2001).

¹⁹ P. Sindzingre, J.-B. Fouet, and C. Lhuillier, *Physical Review B* **66**, 174424 (2002).

²⁰ W. Brenig and A. Honecker, *Phys. Rev. B* **65**, 140407 (2002).

²¹ B. Canals, *Physical Review B* **65**, 184408 (2002).

²² J.-B. Fouet, M. Mambri, P. Sindzingre, and C. Lhuillier, *Phys. Rev. B* **67**, 054411 (2003).

²³ O. Tchernyshyov, O. A. Starykh, R. Moessner, and A. G. Abanov, *Phys. Rev. B* **68**, 144422 (2003).

²⁴ J.-S. Bernier, C.-H. Chung, Y. B. Kim, and S. Sachdev, *Physical Review B* **69**, 214427 (2004).

²⁵ O. A. Starykh, A. Furusaki, and L. Balents, *Phys. Rev. B* **72**, 094416 (2005).

²⁶ Y.-H. Chan, Y.-J. Han, and L.-M. Duan, *Physical Review B* **84**, 224407 (2011).

²⁷ R. Bishop, P. Li, D. Farnell, J. Richter, and C. Campbell, *Physical Review B* **85**, 205122 (2012).

²⁸ N. Shannon, G. Misguich, and K. Penc, *Phys. Rev. B* **69**, 220403 (2004).

²⁹ R. Moessner, O. Tchernyshyov, and S. L. Sondhi, *J. Stat. Phys.* **116**, 755 (2004).

³⁰ O. F. Syljuåsen and S. Chakravarty, *Physical review letters* **96**, 147004 (2006).

³¹ L.-P. Henry, P. C. W. Holdsworth, F. Mila, and T. Roscilde, *Phys. Rev. B* **85**, 134427 (2012).

³² M. Arlego and W. Brenig, *Phys. Rev. B* **75**, 024409 (2007).

³³ R. Ganesh, S. Nishimoto, and J. van den Brink, *Phys. Rev. B* **87**, 054413 (2013).

³⁴ S. Sachdev and R. N. Bhatt, *Phys. Rev. B* **41**, 9323 (1990).

³⁵ M. Isoda and S. Mori, *Journal of the Physical Society of Japan* **67**, 4022 (1998).

³⁶ A. Langari and P. Thalmeier, *Phys. Rev. B* **74**, 024431 (2006).

- ³⁷ H. Rezania, A. Langari, and P. Thalmeier, Phys. Rev. B **77**, 094438 (2008).
- ³⁸ H. Rezania, A. Langari, and P. Thalmeier, Phys. Rev. B **79**, 094401 (2009).
- ³⁹ H. Rezania and A. Langari, Phys. Rev. B **82**, 174407 (2010).
- ⁴⁰ J. Colpa, Physica A: Statistical Mechanics and its Applications **93**, 327 (1978).
- ⁴¹ We remind that according to the plaquette background of POA, the k -space vector runs over the first brillouin zone of an square lattice (set its lattice spacing to 1), constructed from the centers of isolated plaquettes (one every two uncrossed squares) of the checkerboard lattice.
- ⁴² M. S. L. du Croo de Jongh and J. M. J. van Leeuwen, Phys. Rev. B **57**, 8494 (1998).
- ⁴³ J. Rosenfeld and N. E. Ligterink, Phys. Rev. B **62**, 308 (2000).
- ⁴⁴ H. W. J. Blöte and Y. Deng, Phys. Rev. E **66**, 066110 (2002).
- ⁴⁵ Henry and T. Roscilde, Physical review letters **113**, 027204 (2014).
- ⁴⁶ T. Senthil, A. Vishwanath, L. Balents, S. Sachdev, and M. P. A. Fisher, Science **303**, 1490 (2004), <http://www.sciencemag.org/content/303/5663/1490.full.pdf>.